

# Accurate simulations of atomic diffractive scattering from KCl(001) under fast grazing incidence conditions

M. del Cueto<sup>a</sup>, A. S. Muzas<sup>b</sup>, F. Martín<sup>c</sup>, C. Díaz<sup>d,\*</sup>

<sup>a</sup>Department of Chemistry, University of Liverpool, Liverpool L69 3BX, United Kingdom

<sup>b</sup>School of Science, University of New South Wales, Canberra, ACT 2600, Australia

<sup>c</sup>Departamento de Química, Módulo 13, Universidad Autónoma de Madrid, 28049 Madrid, Spain

<sup>d</sup>Departamento de Química Física, Facultad de CC. Químicas, Universidad Complutense de Madrid, 28040 Madrid, Spain

---

## Abstract

Motivated by recent experimental and theoretical results, we have studied the diffraction of atoms (D, <sup>3</sup>He, <sup>4</sup>He) from KCl(001). To perform this study, we have computed continuous potential energy surfaces (PESs) using density functional theory to obtain total interaction energies, with and without taking into account van der Waals forces, and the corrugation reduction procedure. Subsequently, we have performed quantum dynamics simulations using the multi-configuration time-dependent Hartree method. Our simulated spectra compare rather well with those recorded experimentally, specially well for <sup>3</sup>He. The agreement is, in general, better for incidence along the [100] direction. In the case of He projectiles, the inclusion of vdW forces does not systematically improve agreement with the experiment. Finally, in agreement with similar calculations for other systems, we have found that the diffraction spectra are quite sensitive to the subtle characteristics of PES, whereas phonons and electronic excitations seem to play a minor role.

*Keywords:* Grazing incidence, atomic diffractive scattering, quantum dynamics

*PACS:* 34.35.+a, 68.49+Df, 82.65.+r

---

## 1. Introduction

Diffraction of light projectiles from surfaces under fast ( $E_i \approx 0.2 - 20$  keV) grazing incidence ( $1^\circ - 3^\circ$ ) takes place due to the decoupling of the fast motion parallel to the surface and the slow motion perpendicular to it, and to the fact that the perpendicular de Broglie wavelength ( $\lambda_i^\perp$ ) associated with the projectiles is of the same order of magnitude as the surface lattice parameter [1]. Similar to thermal or quasi thermal projectiles diffractive scattering [2, 3], grazing incidence fast atom diffraction (GIFAD) ensures exclusive surface sensitivity of the diffraction patterns. But, contrary to this former technique, GIFAD is not limited by surface temperature, because under these extreme conditions scattering occurs over tens of successive surface atoms which drastically reduces the thermal decoherence [4, 5]. Furthermore, GIFAD can work with normal incidence energies higher than those reached in typical low-energy atomic diffractive scattering experiments (limited by the

nozzle temperature), and therefore it can be used to explore regions of the potential energy surface (PES) that are not accessible in these latter experiments.

GIFAD has been a lively field since 2007, where first experimental measurements were published [6, 7]. This experimental technique has been already used to study a wide variety of systems, insulators [1, 8], semiconductors [9, 10], oxides [11, 12, 13, 14], metals [15, 16, 17, 18], monolayers grown on metal surfaces [19], graphene adsorbed on SiC(0001) [20, 21], reconstructed surfaces [22, 23], and superstructures adsorbed on metal surfaces [24, 25, 26, 27, 28, 29]. In this context, theoretical calculations are called to play a main role in understanding experimental measurements, and describing the physical mechanisms responsible for them. To date, several groups have worked on GIFAD simulations considering both insulating and metal surfaces. For example, in the case of insulators, Aigner et al. [5] employed ab initio quantum trajectory Monte Carlo simulations, in combination with a model two-dimensional PES calculated as the string average along the crystallographic incidence direction of the full PES, calculated at a multiconfiguration self-consistent

---

\*Corresponding author

Email address: crdiaz08@ucm.es (C. Díaz)

field theory level for a large LiF cluster, to reproduce the experimental pattern of GIFAD for He/LiF(001), which allowed them to extract surface buckling information at unique level of details. Taking H/LiF(001) as a benchmark system, Muzas et al. [30] showed, by means of multiconfigurational time-dependent Hartree (MCTDH) quantum dynamics calculations on a density functional theory (DFT) based PES, that GIFAD conditions are satisfied for incidence angles (total energies) much larger (smaller) than the typical ones employed in the experiments. This result means that it is possible to perform accurate theory-experiment comparisons while reducing substantially the computational resources and time. DFT-based potentials, in combination with a wave-packet propagation method, have been used by Debiossac et al. [21] as reference to show that the macroscopic corrugation of the moiré pattern displayed by a monolayer of graphene on SiC(0001) can be fairly well reproduced using a hard-corrugated-wall model, without taking into account soft-wall corrections. GIFAD from insulating surfaces have also been extensively studied by Gravielle and col. These authors have used a surface eikonal approach (SEA) to show, for example, that a proper description of the elastic scattering of He and Ne along the  $\langle 110 \rangle$  LiF(001) crystallographic direction requires a good representation of the polarization potential describing the projectile-surface interaction, whereas along the  $\langle 100 \rangle$  direction the polarization is negligible [31, 32]. Later on [33], they introduced the surface initial value representation approximation (SIVRA) which solves the problem of the rainbow singularities found in their previous SEA-based study, due to a classical description of the atom dynamics. They have also studied the role of van der Waals (vdW) forces in H GIFAD from LiF(001) [34]. Using the SIVRA method, they have shown the minor role that vdW forces play in  $^4\text{He}$  GIFAD from KCl(001). Very recently [35], they have included the effect of the phonons in Ne/LiF(0001) using the semiquantum method Phonon-SIVRA, which introduce the crystal lattice vibrations using a harmonic crystal model. In the case of metal surfaces, Tiwald et al. [17] showed, using Monte Carlo trajectory simulations, that a simple superposition of binary atom-atom potentials fails to describe the interaction of atomic projectiles with aluminum surfaces at GIFAD conditions, only dynamics simulations using PESs based on interpolation of DFT energies showed a satisfactory agreement with experiment. The success of DFT-based PESs to describe atom-metal surface interactions at GIFAD conditions has been further confirmed by Rios et al [18]. These authors have used those kind of potentials and the sur-

face eikonal approximation, which includes the quantum interference between contributions from different projectile-paths, to study He GIFAD from Ag(110). For this system it had also been suggested, using a semiclassical formalism including a friction force in the classical dynamics method, that inelastic electronic processes contribute to GIFAD pattern as a constant background with two maxima at the classical rainbow momentum [36].

In this manuscript, we present the results of a systematic study of GIFAD for D,  $^3\text{He}$ , and  $^4\text{He}$  scattered from KCl(001) for a wide range of normal incidence energies. To perform this study, we have built three continuous PESs by interpolation of DFT energies. In the case of He, we have built two PESs, one including vdW forces and another one without such interactions. Based on these PESs, we have performed quantum dynamics calculations using the MCTDH approach.

## 2. Theoretical approach

### 2.1. PESs construction

Taking into account the low mass and high parallel momentum of the incoming projectiles, and the insulating character of the KCl(001) surface, we have worked within the Born-Oppenheimer static surface (BOSS) framework. The validity of the BO is further supported by GIFAD experiments performed for He,H/LiF(001) [37], which show that electronic excitations play a negligible role for He projectiles. On the other hand, electronic excitations are the dominant mechanism of decoherence for H projectiles. However, as shown in Ref. [37], decoherence does not modify the diffraction patterns, and does not totally suppress diffraction for incidence energies below 1.5 eV. Similar results could be expected for other insulating surfaces. Within the BOSS approximation, all surface atoms are frozen at their equilibrium positions, which means that the only degrees of freedom of the system considered are those of the projectile, i.e., the investigated systems have been described by three-dimensional (3D) PESs. Once the PESs have been built, we have performed quantum dynamics to eventually obtain state-to-state diffraction probabilities.

The continuous PESs, representing the electronic structure of each of the systems studied here, have been built by interpolation of a set of DFT energies, computed at several relevant geometries of the configuration space, using a slightly modified version [38, 39] of the corrugation reducing procedure (CRP) [40]. The DFT energies have been computed using the plane wave

based software package VASP [41, 42, 43, 44]. The interaction of the core electrons with the nuclei has been described within the projector augmented wave (PAW) framework [45, 46]. The plane wave expansion has been limited with a cutoff energy of 550 eV for D/KCl(001), and 750 eV for He/KCl(001). The Brillouin zone has been sampled with a  $3 \times 3 \times 1$  k-point grid. The KCl(001) surface has been modeled by a 5-layer slab, and a  $(2 \times 2)$  unit cell to avoid interactions between the projectile and its periodic images. The interaction between the projectile and the top periodic image of the surface has been minimized by including a  $20 \text{ \AA}$  layer of vacuum in the  $z$  direction, perpendicular to the surface. With these parameters, we have obtained a surface lattice constant,  $a$ , equal to  $4.50 \text{ \AA}$ , in good agreement with the experimental value,  $4.43 \text{ \AA}$  [47]. After relaxation, the interlayer distance and the rumpling, with the  $\text{Cl}^-$  ( $\text{K}^+$ ) ions displaced outwards (inwards), are also in reasonable agreement with previous theoretical calculations [8, 48] and experimental results [47]. The agreement for the top-layer rumpling is specially remarkable, as shown in Table 1. An important issue to take into account when using DFT is the description of the vdW dispersion forces. Standard functionals within the generalized gradient approximation (GGA) do not include explicitly vdW forces, however it has been shown that GGA functionals may yield accurate results for reactive and non-reactive scattering [49, 50] providing that vdW forces do not play an important role in the electronic structure of the system, as expected for D/KCl(001). Thus to build this PES, we have used the standard PBE-GGA functional [61]. However, in the case of the He/KCl(001) PES, it is not clear either to what extent standard GGA functionals yield accurate results, or to what extent the methods available in the literature are able to account properly for the subtle vdW effects associated with He diffraction [52]. Taking into account these uncertainties, we have computed two PESs for He/KCl(001), one based on PBE energies, and another one based on vdW-DF2 [53] energies. We have selected specifically this functional because it has been found previously to give the best description of diffraction of another noble gas, Ne [54]. We have computed DFT energies for 75  $z$  coordinates at 6 different  $(x,y)$  positions for each PES (see Fig. 1). Subsequently, the energies have been interpolated using the modified CRP method. Thus, the 3D PES,  $V^{3D}(\mathbf{R})$ , can be written as:

$$V^{3D}(\mathbf{R}) = J^{3D}(\mathbf{R}) + \sum_{i=1}^n Q^K(R_i)L(R_i) + \sum_{j=1}^m Q^{Cl}(R_j)L(R_j) \quad (1)$$

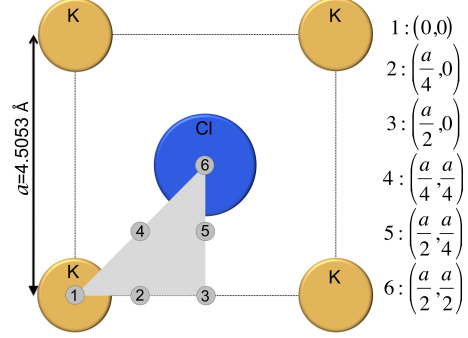


Figure 1: Representation of the irreducible KCl(001) unit cell in light grey. Grey dots indicate the  $(x,y)$  geometries of the 6 positions used in the CRP interpolation.

Table 1: Structural parameters of the KCl(001) surface. Here,  $d$  being the interlayer distance and  $\Delta$  de rumpling. Layers are numbered from the top-most one.

	Layer 1		Layer 2	
	$d(\text{\AA})$	$\Delta(\text{\AA})$	$d(\text{\AA})$	$\Delta(\text{\AA})$
Theory <sup>1</sup>	3.189	0.0325	3.182	0.0047
Theory <sup>2</sup>	—	0.03		
Theory <sup>3</sup>	—	0.025		
Exp. <sup>4</sup>	3.139	0.0286	3.150	-0.00113

<sup>1</sup>This work

<sup>2</sup> Ref. [8]

<sup>3</sup> Ref. [48]

<sup>4</sup> Ref. [47]

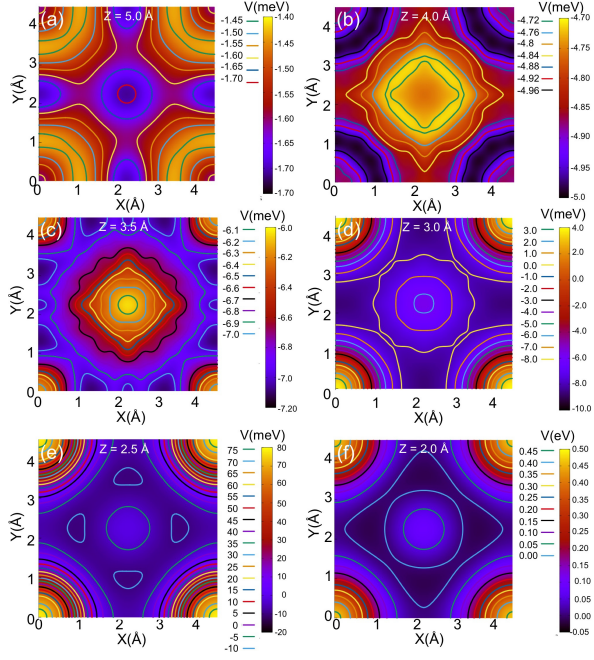


Figure 2: 2D( $x,y$ ) cuts corresponding to the H/KCl(001) PBE-PES. (a)  $z=5.0$  Å with a contour level spacing  $\Delta E=0.05$  meV; (b)  $z=4.0$  Å with  $\Delta E=0.04$  meV; (c)  $z=3.5$  Å with  $\Delta E=0.1$  meV; (d)  $z=3.0$  Å with  $\Delta E=1.0$  meV; (e)  $z=2.5$  Å with  $\Delta E=5.0$  meV; (f)  $z=2.0$  Å with  $\Delta E=0.05$  eV. K and Cl atoms positions are shown in Fig. 1.

with

$$L(z) = \left[ 1 + \exp\left(\frac{z-z_0}{\delta z}\right) \right]^{-1}. \quad (2)$$

Here  $\mathbf{R}$  represent the  $(x, y, z)$ -coordinates vector of the atomic projectiles,  $R_i$  and  $R_j$  are the distances between the projectile and the  $i^{\text{th}}$  K and  $j^{\text{th}}$  Cl surface atom, respectively.  $Q$  is the 1D potential of the projectile atom on top of the  $i^{\text{th}}$  K or  $j^{\text{th}}$  Cl surface atom, and  $J^{3D}(\mathbf{R})$  is the 3D smooth function that has been interpolated in  $z$  using cubic splines, and in  $(x, y)$  with a symmetry-adapted Fourier expansion. According to these equations, far from the surface we interpolate directly  $V^{3D}$ , whereas close to the surface a pure CRP interpolation is applied. For any other intermediate  $z$ -position, the choice of parameters  $\delta z$  and  $z_0$  will control the *amount of CRP* applied to the interpolation. Here, we have used  $z_0=5.0$  Å and  $\delta z=0.21$  Å.

In Fig. 2, we show several 2D( $x, y$ ) cuts displaying the characteristics of the interpolated D/KCl(001) PES. From these plots, we can see that the K-top sites exhibits the highest repulsive potential far from the surface ( $z>5.0$  Å) and close to it ( $z<3.0$  Å), however between 5.0 and 3.0 Å the potential at the Cl-top sites becomes the less attractive. Thus, around the classical turning

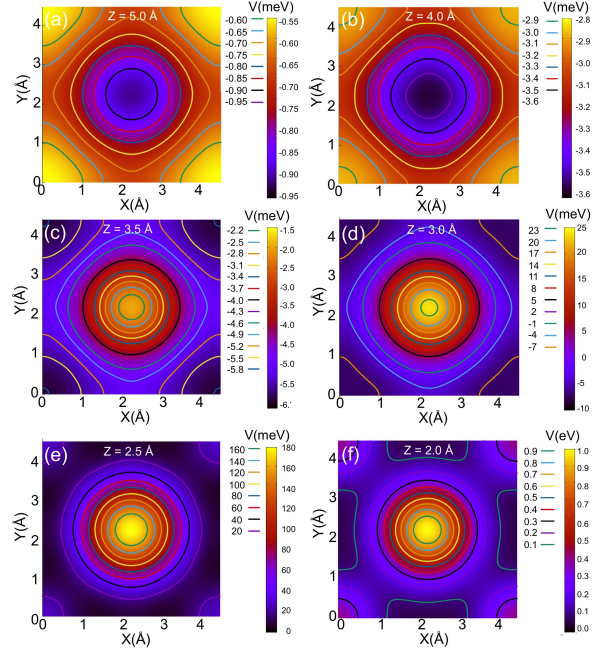


Figure 3: 2D( $x,y$ ) cuts corresponding to the He/KCl(001) PBE-PES. (a)  $z=5.0$  Å with a contour level spacing  $\Delta E=0.05$  meV; (b)  $z=4.0$  Å with  $\Delta E=0.1$  meV; (c)  $z=3.5$  Å with  $\Delta E=0.3$  meV; (d)  $z=3.0$  Å with  $\Delta E=3.0$  meV; (e)  $z=2.5$  Å with  $\Delta E=20$  meV; (f)  $z=2.0$  Å with  $\Delta E=0.1$  eV. K and Cl atoms positions are shown in Fig. 1.

points the potential at K-top and Cl-top sites are very similar.

He projectiles, on the other hand, feel the highest repulsive potential at the K-top sites far from the surface (see Figs. 3 and 4). However the potential at the Cl-top sites increases rather fast, in such a way that at around  $z=3.5$  Å becomes more repulsive than at the K-top sites. Thus, He projectiles, at the typical classical turning points, feels a more repulsive potential at the Cl-top sites. From the comparison between Figs. 3 and 4, we can see that PESs built based on the PBE and vdW-DF2 functional are very similar, and only very subtle differences are observed, therefore only small differences are expected in the diffraction spectra.

## 2.2. Quantum dynamics

We have studied the dynamics by solving the time-dependent Schrödinger equation:

$$\hat{H}\phi(\mathbf{R}, t) = i\frac{\partial\phi(\mathbf{R}, t)}{\partial t}, \quad (3)$$

where

$$\hat{H}^{3D} = -\frac{1}{2M}\left(\frac{\partial^2}{\partial x^2} + \frac{\partial^2}{\partial y^2} + \frac{\partial^2}{\partial z^2}\right) + V^{3D}(\mathbf{R}). \quad (4)$$

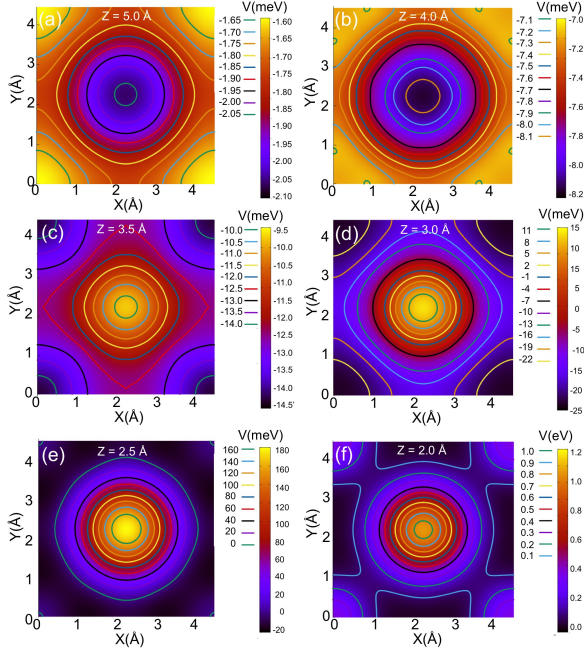


Figure 4: 2D( $x,y$ ) cuts corresponding to the He/KCl(001) vdW-DF2-PES. (a)  $z=5.0$  Å with a contour level spacing  $\Delta E=0.05$  meV; (b)  $z=4.0$  Å with  $\Delta E=0.1$  meV; (c)  $z=3.5$  Å with  $\Delta E=0.5$  meV; (d)  $z=3.0$  Å with  $\Delta E=3.0$  meV; (e)  $z=2.5$  Å with  $\Delta E=20$  meV; (f)  $z=2.0$  Å with  $\Delta E=0.1$  eV; K and Cl atoms positions are shown in Fig. 1.

The solutions of the time-dependent Schrödinger equation have been obtained through the multi configuration time-dependent Hartree (MCTDH) method [55], using the Heidelberg MCTDH package [56]. In the MCTDH framework the time-dependent wave function is represented as a sum of Hartree products of time-dependent single-particle functions (SPFs),  $\varphi_{j_k}^{(k)}$ . Thus the 3D wave function is expressed as:

$$\phi(Q_1, Q_2, Q_3, t) = \sum_{j_1=1}^{n_1} \sum_{j_2=1}^{n_2} \sum_{j_3=1}^{n_3} A_{j_1, j_2, j_3}(t) \prod_{k=1}^3 \varphi_{j_k}^{(k)}(Q_k, t), \quad (5)$$

where  $Q_k$  represents the  $k^{\text{th}}$  mode (in our case mode is equal to degree of freedom), and  $A_{j_1, j_2, j_3}(t)$  are the time-dependent expansion coefficients. The SPFs are in turn expanded in a primitive time-independent basis set:

$$\varphi_{j_k}^{(k)}(Q_k) = \sum_{i_k=1}^{N_k} a_{i_k, j_k}^{(k)}(t) \chi_{i_k}^{(k)}(Q_k). \quad (6)$$

The MCTDH method allows one to calculate state-to-state diffraction probabilities through a flux analysis of

Table 2: MCTDH parameters

Initial wave packet	
Width, $\Delta z$ (Å)	0.40
Position, $z_0$ (Å)	8.50
Grid parameters	
Type $x,y,z$	FFT
$N_x, N_y$	720, 720
$x,y$ -range (Å)	0.00-4.50
$z$ -range (Å)	-0.75-15.00
$N_z$	324
SPFs $x,y,z$	20,20,10
Propagation time (fs)	300-3000
Complex absorbing potential	
$z$ -range (Å)	6.50-15.00
order	2
strength (au)	$1.9 \cdot 10^{-6} - 3.75 \cdot 10^{-5}$

the scattered wave function, once it has been adsorbed by a complex absorbing potential (CAP) located at the non-interacting region. Details about the initial wave packet, SPFs, primitive grid and CAP are given in Table 2.

Eventually, it is also worth noticing that the MCTDH algorithm is more efficient when the potential is expressed as a sum of 1D functions. So thus, we have used the POTFIT algorithm [57, 58] to transform our non-separable 3D PESs into this form. POTFIT approximates the potential as a function of 1D natural potentials  $v_{j_k}$ :

$$V^{3D} \approx V^{app} = \sum_{j_1=1}^{m_1} \sum_{j_2=1}^{m_2} \sum_{j_3=1}^{m_3} C_{j_1, j_2, j_3} v_{j_1}(Q_1) v_{j_2}(Q_2) v_{j_3}(Q_3) \quad (7)$$

where the expansion coefficients,  $C_j$  are calculated as the overlaps between the potential  $V^{3D}$  and the natural potential  $v_j$ . The accuracy of the potential fit can be improved by performing  $N_{iter}$  iterations aiming to improve the potential description inside the relevant dynamical region. In this iterative process, we use a modified reference potential  $\widetilde{V}^{3D}$ , defined as a linear combination of the exact potential  $V^{3D}$  and the fitted potential  $V^{app}$ :

$$\widetilde{V}_{i_1, \dots, i_p}^{3D} = w_{i_1, \dots, i_p} V_{i_1, \dots, i_p}^{3D} + (1 - w_{i_1, \dots, i_p}) V_{i_1, \dots, i_p}^{app}, \quad (8)$$

where  $w$  is a weight function whose value is 1 inside the relevant dynamical region, and  $< 1$  in the rest of the grid. In order to reduce the computational resources used and to avoid numerical inaccuracies in the potential fitting procedure of the repulsive regions, a maximum

Table 3: Parameters used in the POTFIT procedure.  $\Delta_{rms}$  and  $\Delta_{rms}^r$  represent the root-mean-square error in all grid points and in the relevant dynamical region, respectively;  $\max(\epsilon)$  and  $\max(\epsilon)^r$  represent the maximum error in all grid points and in the relevant dynamical region, respectively.

Natural potential basis	
$m_x, m_y, m_z$	60, 60, contr
Relevant dynamical region	
V (eV)	<3.00
$V_{max}$ (eV)	5.00
z (Å)	> 0.00
$N_{iter}$	4
POTFIT accuracy	
$\Delta_{rms}, \Delta_{rms}^r$ (meV)	0.84, 0.05
$\max(\epsilon), \max(\epsilon)^r$ (meV)	53.49, 3.00

potential value  $V_{max}$  was used. In table 3, we show all relevant parameters used in the POTFIT procedure.

### 3. Results and discussion

We have performed dynamics for a wide range of initial normal energies in order to match the range measured experimentally. For that purpose, we have run 11 dynamics simulations for each incidence direction (see Fig. 5), [110] ( $\phi_i = 0^\circ$ ) and [100] ( $\phi_i = 45^\circ$ ). With this number of simulations, we cover the whole normal energy experimental range, 50-600 meV. The corresponding parallel energy for each condition is chosen so that the incidence angle with respect to the surface is kept constant at  $\theta_i = 2^\circ$  ( $E_i^{\parallel} = \frac{E_i^{\perp}}{\sin^2 \theta_i} \cos^2 \theta_i$ ). From our simulations, we can make 3D plots of the diffraction probabilities as a function of the perpendicular incidence energy, and diffraction order,  $n$ . However, to display our results in the same format as the experimental one, we have transformed the  $(n, E_i^{\perp})$  data set into a  $(\Theta, \lambda_i^{\perp})$  data set,  $\Theta$  being the deflection angle, and  $\lambda_i^{\perp}$  the perpendicular incidence de Broglie wavelength associate to the projectile. The relationship between the deflection angles and the diffraction orders is given by the Bragg law for the normal motion,  $d \sin \Theta = n \lambda_i^{\perp}$ , where  $d$  is the channel periodicity at a particular incidence direction. For a better comparison between our simulations, which yield diffraction peak probabilities that are delta functions, and the experimental spectra, we have convoluted our results with 2D Gaussian functions, of widths 3 deg. and 0.025 Å, to simulate the typical width of the experimental peaks.

In Fig. 6, we show the diffraction spectra for D projectiles along the [110] and [100] KCl(001) crystallo-

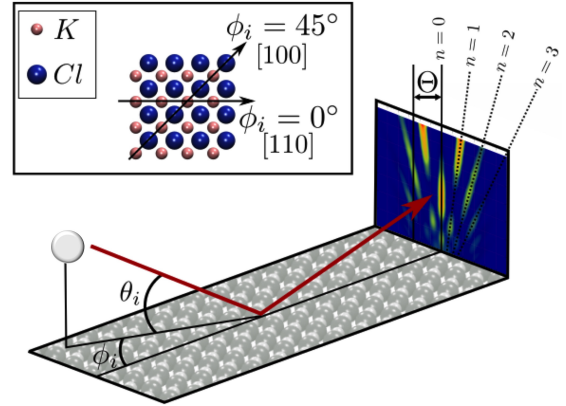


Figure 5: Schematic representation of the diffraction process at grazing incidence of atomic projectiles from a KCl(001) surface, with the projectile path represented in red. We indicate in the detection plane both the deflection angles,  $\Theta$ , and the diffraction orders,  $n$ . The inset shows a top view of the surface, indicating the two incidence directions considered in our study, [110] and [100], as well as their corresponding  $\phi_i$  value.

graphic directions, together with the experimental spectra reported in Ref. [59]. From Fig. 6 left panels, we can see that our theoretical simulations reproduce fairly well the experimental results along the [100] crystallographic direction, in the sense that the same maxima and minima appear at the same  $(\Theta, \lambda_i^{\perp})$  values. This result supports our choice of the PBE DFT functional. As previously shown in the case of He diffraction from metal [52] and semiconducting [60] surfaces the choice of the functional has a decisive influence on the surface corrugation, and therefore on the diffraction spectra. On the other hand, the agreement regarding the relative intensity of diffraction orders is not that satisfactory for  $\lambda_i^{\perp}$  values below 0.8 Å. Although to perform a good comparison between theory and experiment, the experimental diffractograms should be available. The good agreement with experimental results for  $\lambda_i^{\perp} \geq 0.8$  Å contrasts with previous results for H/LiF(001) obtained by Bocan et al [34], which show that the inclusion of vdW effects in the construction of the PES improves the agreement with experimental measurements for  $\lambda_i^{\perp} > 0.4$  Å. However, the corrugation characteristics of these two PESs, H/KCl(001) and H/LiF(001), are quite different, and therefore the role of vdW effects may also be quite different. Regarding the simulated spectra along the [110] direction (Fig. 6 right panels), the agreement with experiment worsens. In this case, the computed relative intensities of the highest diffraction orders are underestimated with respect to the experimental results, and the simulated diffraction patterns are shifted towards

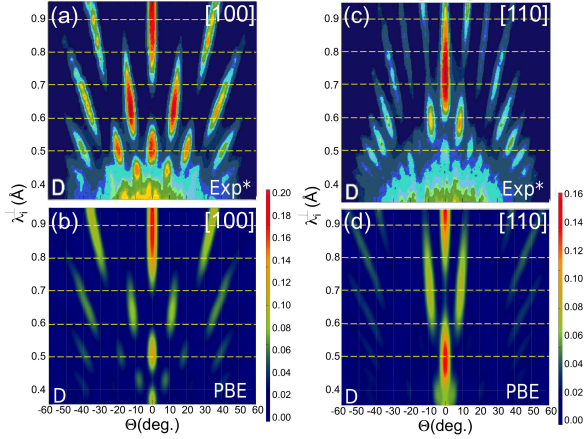


Figure 6: Diffraction spectra of D from KCl(001). Top panels are experimental spectra from Ref [59] and bottom panels simulated theoretical spectra. Left and right panels correspond to incidence along the [100] and [110] crystallographic directions, respectively. The dashed yellow lines are just to guide the eye.

higher  $\lambda_i^\perp$  values with respect to the experimental spectra. A similar shift with respect to the experimental spectra has been previously reported, for example, for H/LiF(001) [30] and  $^4\text{He}/\text{KCl}(001)$  simulated diffraction spectra [48]. As already discussed in Ref. [48] this shift may be due to inaccuracies in the description of the surface rumpling.

We have also performed simulations for  $^3\text{He}$  and  $^4\text{He}$  diffraction (see Figs. 7 and 8). In these cases, as already discussed in Sec. 2.1, anticipating a possible influence of the vdW dispersion forces, we have carried out simulations using two different PESs, one based on the PBE [61] functional and another one based on the vdW-DF2 [53] functional. In this latter functional the effect of dispersion forces are taken into account through a non-local electron correlation correction to the exchange-correlation energy.

Results for  $^3\text{He}$  are shown in Fig. 7. In this case, for both incidence crystallographic directions, [100] (left panels) and [110] (right panels), we observe a quantitative agreement between the experimental results (top-row panels) and our PBE-PES simulations (middle-row panels) with maxima and minima located at almost the same  $(\Theta, \lambda_i^\perp)$  values within the whole energy range studied. However, the relative intensities at  $\lambda_i^\perp$  values below  $0.5 \text{ \AA}$  seem to be underestimated in our simulations. Spectra obtained with the vdW-DF2-PES (bottom-row panels) display a similar overall structure, however a shift towards higher  $\lambda_i^\perp$  is observed. Thank to this shift, the vdW-DF2-PES yields a slightly better agreement with the experiment patterns along the [100] crystallo-

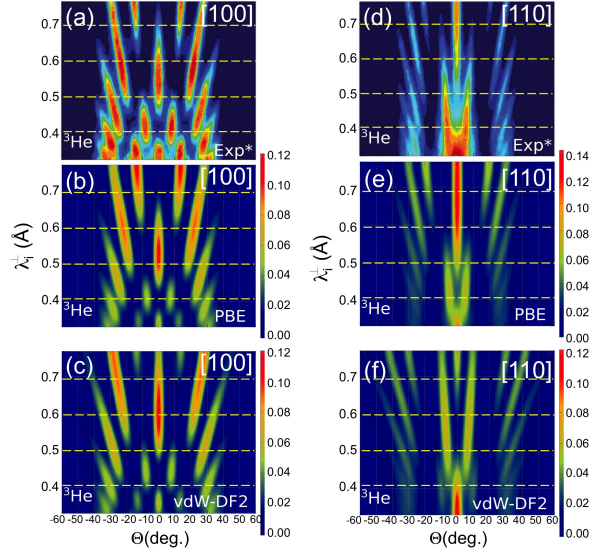


Figure 7: Diffraction spectra of  $^3\text{He}$  from KCl(001). Top panels are experimental spectra from Ref [59], middle panels are simulated theoretical spectra using the PBE-PES, and bottom panels are simulated theoretical spectra using the vdW-DF2-PES. Left and right panels correspond to incidence along the [100] and [110] crystallographic directions, respectively. The dashed yellow lines are just to guide the eye.

graphic direction for  $\lambda_i^\perp$  values below  $0.5 \text{ \AA}$ . On the contrary, in the case of the [110] crystallographic direction, the agreement with the experimental spectrum is worsen respect to PBE-PES results. This is specially apparent for low order diffraction peaks intensity and location for  $\lambda_i^\perp < 0.6 \text{ \AA}$ . These results suggest that the interaction between  $^3\text{He}$  and KCl(001) is, general speaking, better described by the PBE-PES, which agrees with previous results obtained for He/Ru(0001) [52], suggesting that current vdW corrections to DFT, even those describing accurately other noble gas atoms interaction with surfaces [54], overestimate the He/surface interaction. The negligible role of vdW forces in He GIFAD has been previously found, for example, for He diffraction from the  $\beta_2(2 \times 4)$  reconstruction of GaAs(001) [9], for which it was found that quantum simulations using a PES based on PW91 [51] DFT calculations (which do not include vdW effects) reproduce fairly well experimental spectra for perpendicular incidence energies above 30 meV.

At this point, it is also worth pointing out the good agreement between the experimental spectra and PBE simulations for incidence along the [110] crystallographic direction, better than the agreement obtained for H/KCl(001) (see Fig 6 right panels), which seems to indicate that possible inaccuracies in the rumpling description have a lower influence in this case. This

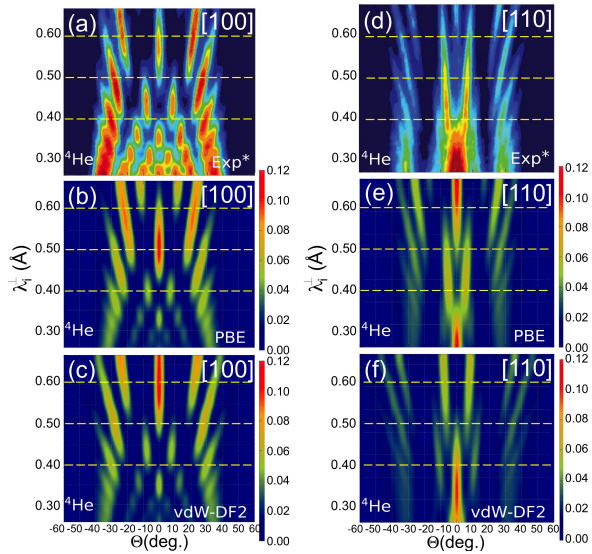


Figure 8: Diffraction spectra of  $^4\text{He}$  from  $\text{KCl}(001)$ . Top panels are experimental spectra from Ref [59], middle panels are simulated theoretical spectra using the PBE-PES, and bottom panels are simulated theoretical spectra using the vdW-DF2-PES. Left and right panels correspond to incidence along the  $[100]$  and  $[110]$  crystallographic directions, respectively. The dashed yellow lines are just to guide the eye.

is probably due to the fact that the average classical turning point for  $^3\text{He}$  is located further away from the  $\text{KCl}(001)$  surface than that for D, and therefore,  $^3\text{He}$  is scattered from a region of the PES where the rumpling is hardly felt by the projectile.

In Fig. 8, we show results for  $^4\text{He}/\text{KCl}(001)$ . In this case, the simulated spectra based on the the PBE-PES reproduce the experimental measurements within a small shift towards smaller  $\lambda_i^\perp$ , similar for both crystallographic directions. Thus, our PBE-PES reproduces a little worse the experimental spectra for  $^4\text{He}$  than for  $^3\text{He}$ . On the other hand, the theoretical spectra simulated based on the vdW-DF2-PES are similar to those obtained from the PBE-PES, but shifted towards higher  $\lambda_i^\perp$  values, in such a way that along the  $[110]$  incidence direction vdW-DF2 spectra reproduce pretty well the experimental ones, whereas along the  $[100]$  direction vdW-DF2 spectra are clearly shifted towards higher  $\lambda_i^\perp$  values with respected to experimental spectra.

It is also worth comparing our results for  $^4\text{He}/\text{KCl}(001)$ , with previous theoretical simulations available in the literature [48]. These latter simulations were carried out using the semi-quantum approach SIVR and a PBE-DFT based PES. Interestingly, spectra shown in Ref. [48] resemble our vdW-DF2 spectra more than our PBE spectra. As the PBE-PES used in Ref. [48] was also built using the

corrugation reducing procedure, the differences found can only be due to either the different parameters used in the DFT calculations, leading to slightly different surface parameters (lattice constant and rumpling), or to different dynamics methods used to calculate the diffraction probabilities. Taking into account that small changes in the corrugation of the PES lead to measurable changes in the diffraction spectra, it seems plausible to point to the slightly different surface parameters as the source of the differences observed between our PBE spectra and those from Ref. [48].

#### 4. Conclusions

We have carried out MCTDH quantum dynamics simulations for D and He diffraction from  $\text{KCl}(001)$  under GIFAD conditions as a function of the normal incidence energy, using DFT-based PESs. From the, generally speaking, rather good agreement between our simulated spectra and the, previously recorded, experimental spectra, we can draw some interesting conclusions:

- In line with previous GIFAD results for other atom-surface systems, we have found that DFT-based PESs describe rather well the interaction of D and He projectiles with  $\text{KCl}(001)$ .
- Regarding the role of van der Waals forces, our results seem to indicate that either these forces play a minor role in He GIFAD or the vdW-DF2 DFT functional, which has shown to describe reasonably well molecule- and atom-surface interactions with a strong vdW component, fails to reproduce weak vdW interactions. At this point, we should also remark that the very good results obtained with PBE, a functional that does not include a proper description of vdW forces, may be due to an errors cancelation.
- Taking into account that we have worked within the static surface approximation, we can safely conclude that the effect of phonons and/or energy exchange between the projectile and the surface is negligible, or at least, that it does not change substantially the relative intensity of diffraction peaks.
- In view to the good agreement between our adiabatic simulations and the experimental results, we can also conclude that electronic excitations, although are expected to be present in the experiments due to the highly energetic collisions, do not affect significantly the relative intensity of diffraction peaks.

Finally, we should point out that a more accurate comparison between theoretical simulations and experimental results will require the knowledge of the experimental diffractograms. We hope that our work will stimulate further experimental works to make diffractograms available.

## 5. Acknowledgements

This work has been supported by the MINECO Project FIS2016-77889-R. C. Díaz acknowledges the Ramón y Cajal program of the MINECO. M. del Cueto acknowledges the FPI program of the MINECO co-financed by the European Social Fund. This work was undertaken with the assistance of resources and services from CCC-UAM.

## References

- [1] H. Winter, A. Schüller, *Prog. Surf. Sci.* 86 (2011) 169.
- [2] D. Farías, K. H. Rieder, *Rep. Prog. Phys.* 61 (1998) 1575.
- [3] D. Farías, R. Miranda, *Prog. Surf. Sci.* 86 (2011) 222.
- [4] J. R. Manson, H. Khemliche, P. Rocin, *Phys. Rev. B* 78 (2008) 155408.
- [5] F. Aigner, N. Simonovic, B. Solleder, J. Wirtz, J. Burgdörfer, *Phys. Rev. Lett.* 101 (2008) 253201.
- [6] A. Schüller, S. Wethekam, H. Winter, *Phys. Rev. Lett.* 98 (2007) 016103.
- [7] P. Rousseau, H. Khemliche, A. G. Borisov, P. Rocin, *Phys. Rev. Lett.* 98 (2007) 016104.
- [8] U. Specht, M. Busch, J. Seifert, A. Schüller, H. Winter, C. Gärtner, R. Włodarczyk, M. Sierra, J. Sauer, *Nucl. Instrum. Meth. Phys. Res. B*, 269 (2011) 799.
- [9] M. Debiossac, A. Zugarramurdi, H. Khemliche, P. Rocin, A. G. Borisov, A. Momeni, P. Atkinson, M. Eddrief, F. Finocchi, V. H. Etgens, *Phys. Rev. B* 90 (2014) 155308.
- [10] P. Rocin, M. Debiossac, *Phys. Rev. B* 96 (2017) 035415.
- [11] M. Busch, J. Seifert, E. Meyer, H. Winter, *Phys. Rev. B* 86 (2012) 241402.
- [12] A. Schüller, D. Blauth, J. Seifert, M. Busch, H. Winter, K. Gärtner, R. Włodarczyk, J. Sauer, M. Sierka, *Surf. Sci.* 606 (2012) 161.
- [13] M. Busch, J. Seifert, E. Meyer, H. Winter, *Nucl. Instrum. Methods Phys. Res. B* 317 (2013) 90.
- [14] M. Busch, E. Meyer, K. Irmscher, Z. Galazka, K. Gärtner, H. Winter, *Appl. Phys. Lett.* 105 (2014) 051603.
- [15] N. Bundaleski, H. Khemliche, P. Soullisse, P. Rocin 101 (2008) 177601.
- [16] M. Busch, A. Schüller, S. Wethekam, H. Winter, *Surf. Sci.* 603 (2009) L23.
- [17] P. Tiwald, A. Schüller, H. Winter, K. Tökesi, F. Aigner, S. Gräfe, C. Lemell, J. Burgdörfer, *Phys. Rev. B* 82 (2010) 125453.
- [18] C. A. Ríos-Rubiano, G. A. Bocan, M. S. Gravielle, N. Bundaleski, H. Khemliche, P. Rocin, *Phys. Rev. A* 87 (2013) 012903.
- [19] J. Seifert, A. Schüller, H. Winter, R. Włodarczyk, J. Sauer, M. Sierka, *Phys. Rev. B* 82 (2010) 035436.
- [20] A. Zugarramurdi, M. Debiossac, P. Lunca-Popa, A. J. Mayne, A. Momeni, A. G. Borisov, Z. Mu, P. Rocin, H. Khemliche *Appl. Phys. Lett.* 106 (2015) 101902.
- [21] M. Debiossac, A. Zugarramurdi, Z. Mu, P. Lunca-Popa, A. J. Mayne, P. Rocin, *Phys. Rev. B* 94 (2016) 205403.
- [22] H. Khemliche, P. Rousseau, P. Rocin, V. H. Etgens, F. Finocchi, *Appl. Phys. Lett.* 95 (2009) 151901.
- [23] M. Debiossac, P. Atkinson, A. Zugarramurdi, M. Eddrief, F. Finocchi, V. H. Etgens, A. Momeni, H. Khemliche, A. G. Borisov, P. Rocin, *Appl. Surf. Sci.* 391 (2017) 53.
- [24] J. Seifert, H. Winter, *Surf. Sci.* 603 (2009) L109.
- [25] A. Schüller, M. Busch, J. Seifert, S. Wethekam, H. Winter, K. Gärtner, *Phys. Rev. B* 79 (2009) 235425.
- [26] J. Seifert, H. Winter, *Phys. Rev. Lett.* 108 (2012) 065503.
- [27] J. Seifert, M. Busch, E. Meyer, H. Winter, *Phys. Rev. Lett.* 111 (2013) 137601.
- [28] J. Seifert, M. Busch, E. Meyer, H. Winter, *Phys. Rev. B* 89 (2014) 075404.
- [29] N. Kalashnyk, H. Khemliche, P. Rocin, 364 (2016), 235.
- [30] A. S. Muzas, F. Gatti, F. Martín, C. Díaz, *Nucl. Instrum. Meth. B* 382 (2016) 49.
- [31] M. S. Gravielle, J. E. Miraglia, *Phys. Rev. A* 78 (2008) 022901.
- [32] M. S. Gravielle, A. Schüller, H. Winter, J. E. Miraglia, *Nucl. Instr. Meth. Phys. Res. B* 269 (2011) 1208.
- [33] M. S. Gravielle, J. E. Miraglia, *Phys. Rev. A* 90 (2014) 052718.
- [34] G. A. Bocan, J. D. Fuhr, M. S. Gravielle, *Phys. Rev. A* 94 (2016) 022711.
- [35] L. Frisco, M. S. Gravielle, *Phys. Rev. A.* 100 (2019) 062703.
- [36] C. A. Ríos-Rubiano, G. A. Bocan, J. I. Juaristi, M. S. Gravielle, *Phys. Rev. A* 89 (2014) 032706.
- [37] J. Lienemann, A. Schüller, D. Blauth, J. Seifert, S. Wethekam, M. Busch, K. Maass, H. Winter, *Phys. Rev. Lett.* 106 (2011) 067602.
- [38] A. S. Muzas, F. Martín, C. Díaz, *Nucl. Instr. Meth. Phys. Res. B* 354 (2015) 9.
- [39] A. S. Muzas, M. del Cueto, F. Gatti, M. F. Somers, G. J. Kroes, F. Martín, C. Díaz, *Phys. Rev. B* 96 (2015) 205432.
- [40] H. F. Busnengo, A. Salin, W. Dong, *J. Chem. Phys.* 112 (2000) 7641.
- [41] G. Kresse, J. Hafner, *Phys. Rev.* 47 (1993) 558.
- [42] G. Kresse, J. Hafner, *Phys. Rev.* 49 (1994) 14251.
- [43] G. Kresse, J. Furthmuller, *Phys. Rev.* 54 (1996) 1758.
- [44] G. Kresse, J. Furthmuller, *Comp. Mater. Sci.* 6 (1996) 15.
- [45] P. Blochl, *Phys. Rev. B.* 50 (1994) 17953.
- [46] G. Kresse, D. Joubert, *Phys. Rev. B.* 59 (1999) 1758.
- [47] J. Vogt, H. Weiss, *Surf. Sci.* 491 (2001) 155.
- [48] G. A. Bocan and M. S. Gravielle, *Nucl. Instrum. Meth. B* 421 (2018) 1.
- [49] P. Nieto, E. Pijper, D. Barredo, G. Laurent, R. A. Olsen, E. J. Baerends, K. J. Kroes, F. Farías, *Science* 312 (312) 86.
- [50] C. Díaz, E. Pijper, R. A. Olsen, H. F. Busnengo, D. J. Auerbach, G. J. Kroes. *Science* 326 (2010) 11192.
- [51] J. P. Perdew, J. A. Cherary, Z. H. Vosko, K. A. Jackson, M. R. Pederson, D. J. Singh, C. Fiolhais, *Phys. Rev. B* 46 (1992) 6671.
- [52] M. del Cueto, J. M Reinhard, A. Al Taleb, D. Farís, F. Martín, C. Díaz, *J. Phys.: Condens. Matter*, 31 (2009) 135901.
- [53] K. Lee, E. D Murray, L. Kong, B. I. Lundqvist, D. C. Langreth, *Phys. Rev. B* 82 (2010) 081101.
- [54] M. del Cueto, A. S Muzas, G. Fuchsels, F. Gatti, F. Martín, C. Díaz, *Phys. Rev. B* 93 (2016) 060301.
- [55] M. H. Beck, A. Jäckle, G. A. Worth, H. D Meyer, *Phys. Rep.* 324 (2000) 1.
- [56] G. A. Worth, M. H. Beck, A. Jäckle, H. D Meyer, Version 8.4 (2007) See <http://mctdh.uni-hd.de/>, University of Heidelberg, Germany.
- [57] A. Jäckle, H. D. Meyer, *J. Chem. Phys.* 104 (1996) 7974.
- [58] A. Jäckle, H. D Meyer, *J. Chem. Phys.* 109 (1998) 3772.
- [59] E. Meyer, PhD thesis, Humboldt-Universität zu Berlin (2016).

- [60] M. del Cueto, A. S. Muzas, T. J. Frankcombe, F. Martín, C. Díaz, *Phys. Chem. Chem. Phys.* 21 (2019) 15879.
- [61] J. P. Perdew, K. Burke, M. Ernzerhof, *Phys. Rev. Lett.* 77 (1996) 3865.